


RESEARCH ARTICLE

Open Access



# Effervescent cannabidiol solid dispersion-doped dissolving microneedles for boosted melanoma therapy via the “TRPV1-NFATc1-ATF3” pathway and tumor microenvironment engineering

Jiachen Shi<sup>1†</sup>, Qiuling Ma<sup>1†</sup>, Wenting Su<sup>1</sup>, Congyan Liu<sup>1,2</sup>, Huangqin Zhang<sup>1,2</sup>, Yuping Liu<sup>1,2</sup>, Xiaoqi Li<sup>1,2</sup>, Xi Jiang<sup>1</sup>, Chang Ge<sup>1</sup>, Fei Kong<sup>1</sup>, Yan Chen<sup>1,2</sup> and Ding Qu<sup>1,2\*</sup> 

## Abstract

**Background** Conventional dissolving microneedles (DMNs) face significant challenges in anti-melanoma therapy due to the lack of active thrust to achieve efficient transdermal drug delivery and intra-tumoral penetration.

**Methods** In this study, the effervescent cannabidiol solid dispersion-doped dissolving microneedles (Ef/CBD-SD@DMNs) composed of the combined effervescent components (CaCO<sub>3</sub> & NaHCO<sub>3</sub>) and CBD-based solid dispersion (CBD-SD) were facilely fabricated by the “one-step micro-molding” method for boosted transdermal and tumoral delivery of cannabidiol (CBD).

**Results** Upon pressing into the skin, Ef/CBD-SD@DMNs rapidly produce CO<sub>2</sub> bubbles through proton elimination, significantly enhancing the skin permeation and tumoral penetration of CBD. Once reaching the tumors, Ef/CBD-SD@DMNs can activate transient receptor potential vanilloid 1 (TRPV1) to increase Ca<sup>2+</sup> influx and inhibit the downstream NFATc1-ATF3 signal to induce cell apoptosis. Additionally, Ef/CBD-SD@DMNs raise intra-tumoral pH environment to trigger the engineering of the tumor microenvironment (TME), including the M1 polarization of tumor-associated macrophages (TAMs) and increase of T cells infiltration. The introduction of Ca<sup>2+</sup> can not only amplify the effervescent effect but also provide sufficient Ca<sup>2+</sup> with CBD to potentiate the anti-melanoma efficacy. Such a “one stone, two birds” strategy combines the advantages of effervescent effects on transdermal delivery and TME regulation, creating favorable therapeutic conditions for CBD to obtain stronger inhibition of melanoma growth in vitro and in vivo.

**Conclusions** This study holds promising potential in the transdermal delivery of CBD for melanoma therapy and offers a facile tool for transdermal therapies of skin tumors.

<sup>†</sup>Jiachen Shi and Qiuling Ma contributed equally to this work.

\*Correspondence:  
Ding Qu  
quding1985@hotmail.com

Full list of author information is available at the end of the article



© The Author(s) 2023. **Open Access** This article is licensed under a Creative Commons Attribution 4.0 International License, which permits use, sharing, adaptation, distribution and reproduction in any medium or format, as long as you give appropriate credit to the original author(s) and the source, provide a link to the Creative Commons licence, and indicate if changes were made. The images or other third party material in this article are included in the article's Creative Commons licence, unless indicated otherwise in a credit line to the material. If material is not included in the article's Creative Commons licence and your intended use is not permitted by statutory regulation or exceeds the permitted use, you will need to obtain permission directly from the copyright holder. To view a copy of this licence, visit <http://creativecommons.org/licenses/by/4.0/>. The Creative Commons Public Domain Dedication waiver (<http://creativecommons.org/publicdomain/zero/1.0/>) applies to the data made available in this article, unless otherwise stated in a credit line to the data.

**Keywords** Dissolving microneedles, Melanoma, Cannabidiol, Effervescent, Tumor microenvironment,  $\text{Ca}^{2+}$  influx

## Background

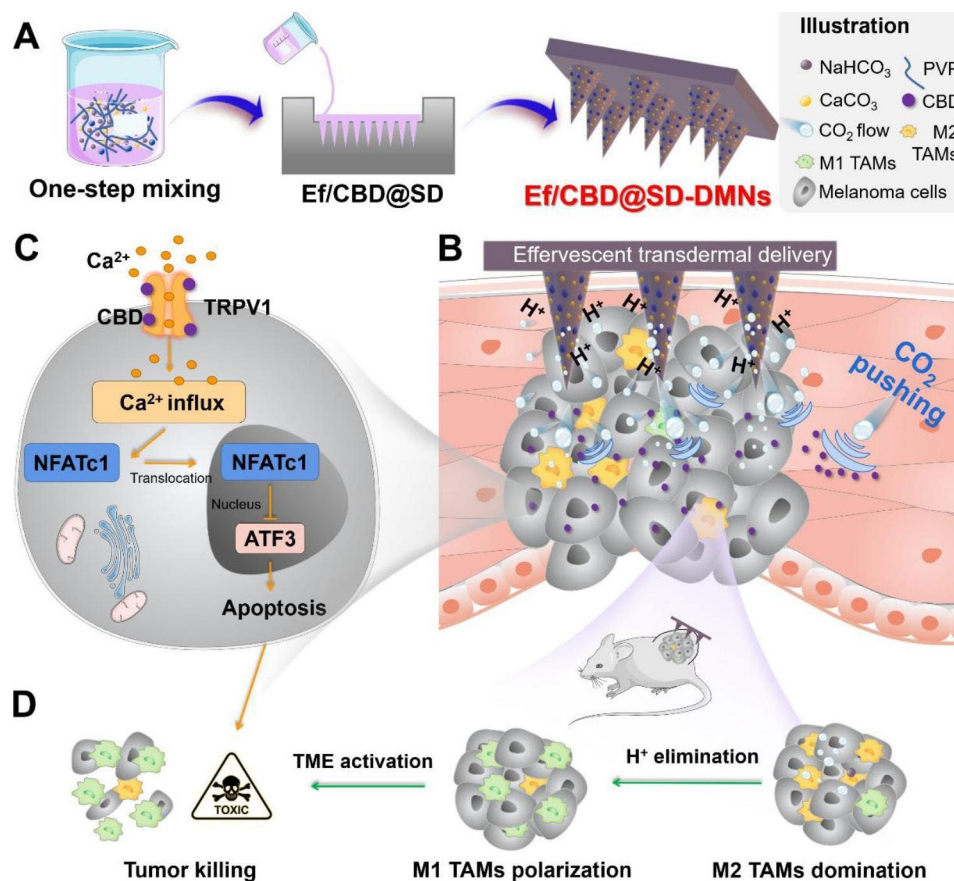
Melanoma, a rare skin cancer originating from melanocytes, accounts for only approximately 1% of all skin tumors but is considered the most lethal due to its high invasiveness [1]. Chemotherapy remains the most significant adjuvant therapy following surgical resection; however, its effectiveness in treating melanoma patients is controversial due to severe systemic toxicity and poor tumor targeting [2]. Transient receptor potential vanilloid (TRPV), an ion channel protein involved in regulating intracellular calcium ion concentration, plays a crucial role in melanoma. Studies have shown that the activation of TRPV can affect survival and proliferation of melanoma cells (A2058 and A375) by altering the intracellular and extracellular  $\text{Ca}^{2+}$  concentration [3–5], making it one of the most promising targets for melanoma therapy [6]. Cannabidiol, as a TRPV1 agonist, can activate the TRPV1 channel by changing the conformation of the channel protein, leading to the opening of the channel pore and allowing the influx of  $\text{Ca}^{2+}$  [7]. Previous studies have demonstrated that the influx of  $\text{Ca}^{2+}$  triggers the “ $\text{Ca}^{2+}$  influx-NFATc1-ATF3” downstream signaling pathway that involved in the melanoma development [3]. However, the correlation between CBD and “ $\text{Ca}^{2+}$  influx-NFATc1-ATF3” pathways has not been established. Furthermore, CBD is an extremely water-insoluble compound with some non-ignorable drawbacks, such as low oral bioavailability and poor thermal stability [8]. Therefore, designing a suitable CBD-associated formulation for the treatment of melanoma is highly desired from the perspective of drug delivery.

The stratum corneum, which is the outermost layer of human skin, consists of 15–20 layers of fat-depleted and protein-rich keratinocytes that serve as the primary barrier to protect the skin from foreign substances [3]. Microneedle-mediated transdermal drug delivery can overcome the obstacles presented by the stratum corneum, delivering drugs directly to topical lesions and thereby improving transdermal delivery efficiency [9–11]. This makes microneedles a promising tool for delivering active ingredients in the treatment of melanoma [12–14]. Microneedle delivery systems can be classified according to their matrices and preparation technologies, including dissolving microneedles (DMNs) [15], coated microneedles [16], hollow microneedles [17], solid microneedles [18], and others. DMNs are the self-absorbed device that no further actions are needed after the administration, gradually becoming the preferred type for microneedle designs [19]. However, DMNs face certain challenges in directly loading hydrophobic CBD because their matrix is hydrophilic [20]. Assembling CBD as a water-soluble

module in advance is a potential approach to fabricating CBD-loaded DMNs. With the rapid development of materials science, there are now various mature technologies available for hydrophilizing CBD, such as solid dispersions [21], microemulsions [22], liposomes [23], electrospun fibers [24], and more. Polyvinyl pyrrolidone (PVP) has been employed in both the preparation of solid dispersions [25–27] and DMNs [28, 29], indicating a potential matrix candidate for assembling CBD-associated DMNs.

Effective transdermal drug delivery relies on deep penetration into the skin. Effervescent compounds, which produce gas under specific conditions, might be a solution for achieving deep penetration. The gas bubbles generated by effervescent components create temporary pores or channels through which drugs can diffuse into the deeper layers of the skin. Miguel and coworkers [30] reported on a strategy of active penetration-boosting by producing hydrogen bubbles inside the tumor tissues based on the reaction between magnesium particles and intra-tumoral protons. Likewise, Ke and coworkers [31] designed a microneedle system that incorporates sodium bicarbonate ( $\text{NaHCO}_3$ ) and rapidly forms  $\text{CO}_2$  bubbles to separate the adhesive backing and drug-loaded arrays after skin insertion. These studies demonstrate that such bubble-produced strategies are capable of actively pushing the drug deep permeation, highlighting the promising prospects in topical drug delivery. Melanoma is characterized by a mildly acidic microenvironment, which not only creates favorable conditions for effervescent compounds to produce gas but also contributes to the deterioration of the tumor microenvironment (TME) by reducing the viability and proliferation of immune cells [32–34]. In addition, some effervescent components, such as  $\text{NaHCO}_3$  and  $\text{CaCO}_3$ , can act as intra-tumoral pH regulators by neutralizing excess protons and increasing the concentration of bicarbonate and bicarbonate ions [35–37], resulting in the M1 repolarization of tumor-associated macrophages (TAMs) [38] and activating the entire TME [39, 40]. Therefore, effervescent components are potentially suitable for the design of multi-functional DMNs for the comprehensive treatment of melanoma.

Herein, we developed CBD solid dispersion-based effervescent DMNs (Ef/CBD-SD@DMNs) for deep transdermal delivery and enhanced melanoma therapy. As illustrated in Scheme 1, Ef/CBD-SD@DMNs are readily fabricated by combining CBD solid dispersion (CBD-SD) and effervescent components ( $\text{NaHCO}_3 + \text{CaCO}_3$ ) through the “one-step micro-molding” method. When pressed into the skin, Ef/CBD-SD@DMNs burst  $\text{CO}_2$  bubbles to push the CBD toward the tumors. With a



**Scheme 1** Schematic illustration of fabrication, active transdermal delivery, and synergistic antitumor mechanism of Ef/CBD-SD@DMNs. The CO<sub>2</sub> bubbles generated by the combined effervescent components (CaCO<sub>3</sub> & NaHCO<sub>3</sub>) push CBD deep penetration, consequently improving transdermal and tumoral delivery. The Ca<sup>2+</sup> influx on one hand triggers the “TRPV1-NFATc1-ATF3” pathway for melanoma apoptosis and on the other hand results in the engineering of the tumor microenvironment, collaboratively boosting anti-melanoma therapy

sufficient supply of Ca<sup>2+</sup> from CaCO<sub>3</sub>, CBD activates TRPV1 to induce melanoma apoptosis via the “Ca<sup>2+</sup> influx-NFATc1-ATF3” pathway. Meanwhile, the effervescent components raise the intra-tumoral pH, leading to M1 repolarization of the TAMs and thereby relieving the immunosuppressive TME. Such a “one stone, two birds” effervescent design not only improves transdermal delivery of CBD but also creates favorable conditions for CBD to boost the anti-melanoma efficacy. This study focuses on the preparation, characterizations, transdermal delivery, tumoral penetration, antitumor efficacy, and TME characterizations by Ef/CBD-SD@MNs. This study has promising potential in using transdermal CBD delivery for melanoma therapy and provides a straightforward tool for transdermal therapy of skin tumors.

## Materials and methods

### Materials

CaCl<sub>2</sub> (purity: 96%) and ethanol (purity: 98%) were purchased from Guangdong Xilong Scientific Co., Ltd. Cannabidiol (CBD; purity: 99%), polyvinylpyrrolidone (PVP; average Mw: 1,300,000, K88-96), NaHCO<sub>3</sub> (purity > 99%),

CaCO<sub>3</sub> (purity: 98%; size: ≤ 50 nm), and coumarin 6 (C6) were purchased from Shanghai Aladdin Biochemical Technology Co., Ltd. Acetonitrile was purchased from Anhui Tedia High Purity Solvents Co., Ltd. Tween 80 (water content: ≤ 3%) was purchased from Guangzhou saiguobio biotech Co., Ltd. Propidium Iodide was purchased from KeyGEN (Nanjing, China). Ultrapure water was acquired via ElixEssential system (Millipore, Shanghai, China). Other chemicals were used of analytical grade.

### Cell culture

Melanoma cells (B16-F10) were purchased from the National Collection of Authenticated Cell Cultures (Shanghai, China) and cultured in Dulbecco’s Modified Eagle’s Medium (DMEM) containing 10% fetal bovine serum (FBS), 1% penicillin (100 U/mL) and streptomycin (100 mg/mL) in a cell incubator (Thermo Fisher, USA) at 37°C with 5% CO<sub>2</sub> and 90% humidity. Calcium-free DMEM was purchased from Yuchun BioTech Co., Ltd. (Shanghai, China). 0.3 mmol/L, 2 mmol/L, and 10 mmol/L CaCl<sub>2</sub> was added into calcium-free DMEM to

obtain  $\text{Ca}^{2+}$  (low) DMEM,  $\text{Ca}^{2+}$  (medium) DMEM,  $\text{Ca}^{2+}$  (high) DMEM, respectively.

### Animals

Healthy male C57BL/6J mice weighing  $20 \pm 2$  g were provided and raised by the Animal Experiment Center of Jiangsu Province Academy of Traditional Chinese Medicine, and all animal experiments met the ethical requirements stipulated by the National Experimental Animal Center.

### Preparation of Ef/CBD-SD@DMNs

20 mg of CBD, 111.11 mg of PVP, 20 mg of  $\text{CaCO}_3$ , and 16.8 mg of  $\text{NaHCO}_3$  were dissolved in 1 mL of ethanol and strongly stirred at 600 rpm for 30 min. The mixture solution was cast into a microneedle mold ( $12 \times 12$  arrays; length 1000  $\mu\text{m}$ ; diameter 460  $\mu\text{m}$ ) and centrifuged at 4500 rpm for 15 min, followed by drying thoroughly at room temperature to obtain Ef/CBD-SD@DMNs.  $\text{NaHCO}_3$ /CBD-SD@DMNs or CBD-SD@DMNs was prepared by the similar method mentioned above but without  $\text{CaCO}_3$  or  $\text{CaCO}_3$ & $\text{NaHCO}_3$ .

### Characterizations of Ef/CBD-SD@DMNs

The DMNs were measured with an X-ray diffractometer (Rigaku, Japan) using  $\text{Cu K}\alpha$  radiation at a tube voltage of 40 kV, a current of 40 mA, and a scan  $2\theta$  angle range of  $3 \sim 40^\circ$ . The scanning speed was set at 0.1s/step with a step size of  $0.02^\circ$ . The DMNs samples to be tested were sprayed conductive coating and imaged using a scanning electron microscope (SEM, LEO 1530VP, Germany) equipped with an energy-dispersive X-ray spectroscopy (EDS, Germany). The DMNs were also cut into single rows and taken images using a fluorescence inverted microscope (IX73, Olympus, Japan). The mechanical property was tested by a pressure tester (Mark-10, USA), a cylindrical probe with a diameter of 10 mm compressed the microneedle arrays at a rate of 10.5 mm/min, and the force-displacement of the arrays was recorded to plotted the force-distance curve. The dynamic processes of Ef/CBD-SD@DMNs dissolving in different mediums were recorded by a fluorescence inverted microscope (IX73, Olympus, Japan).

### Isolation of mice skin

The mice were anesthetized with intramuscular administration of 50% ethyl carbamate solution (50 mg/kg), and the hair was shaved with an electric razor and then removed completely by a depilatory paste. After being sacrificed, the abdominal skin of the mice was isolated, followed by removing the subcutaneous tissues and washing it with saline thrice.

### Skin permeation

Pig skin was purchased from a nearby wet market. The DMNs were pressed into the excised pig skin for 5 min. After removal of the DMNs, a part of the treated skin was fixed with 4% paraformaldehyde for 48 h, dehydrated, embedded in paraffin, and prepared the section, successively. After being stained with hematoxylin and eosin (H&E), the slice was observed with a microscope (IX73, Olympus, Japan).

### Chromatographic conditions of CBD

CBD was determined at  $37^\circ\text{C}$  by an Agilent 1260 Infinity instrument (Agilent Technologies Inc., Santa Clara, CA, USA) with the ZORBAX SB-C18 column ( $250 \times 4.6$  mm, 5  $\mu\text{m}$ ) eluted with deionized water-acetonitrile (35/65, v/v) at a flow of 1 mL/min and a detection wavelength at 220 nm. The linear regression equation with drug concentration as the independent variable and peak area as the dependent variable was  $y = 28.407x + 65.452$  ( $r = 0.9998$ ) in the range of 2 ~ 512  $\mu\text{g/mL}$ .

### Dissolution test

100 mL of phosphate buffer containing Tween 80 (1%) was degassed and added to a dissolution tester (ZRS-8G, Tianjin, China). The DMNs were separately added into the medium with different pH values, followed by stirring the medium at 100 rpm at  $(37.0 \pm 0.5)^\circ\text{C}$ . The mediums were collected at the predetermined time intervals, the same volume of fresh medium was immediately replenished. The samples were centrifuged at 13,000 rpm for 15 min and the supernatant was harvested to detect by HPLC. Cumulative dissolution amount ( $\mu\text{g}$ ) =  $C_d \times V_m$ , where  $C_d$  and  $V_m$  are the accumulative content of CBD in the dissolution cups and the volume of the medium, respectively. Every experiment was performed in triplicate.

### Transdermal Penetration and Retention in vitro

A piece of freshly-isolated mice abdominal skin was fixed in a Franz diffusion instrument (TK-24BL, Shanghai, China) with the cross-sectional area of the Franz diffusion cell of  $0.785 \text{ cm}^2$ . The stratum corneum of the skin was facing the supply cell and the PBS solutions with different pH values were in the receiving cell. The DMNs were rapidly pressed into the skin, followed by stirring the receiving medium at 250 rpm at  $37^\circ\text{C}$ . The mediums were collected at the predetermined time intervals. At the end of the transdermal studies, the skin was rinsed with saline thrice and grinded into homogenates solution (with 1% Tween 80 PBS), followed by centrifuging at 13,000 rpm for 15 min. The supernatant was harvested to detect by HPLC. Transdermal flux was calculated as the following equation. Transdermal flux ( $\mu\text{g}/\text{cm}^2$ ) =  $C_t/S_F$ , where  $C_t$  and  $S_F$  are the accumulative



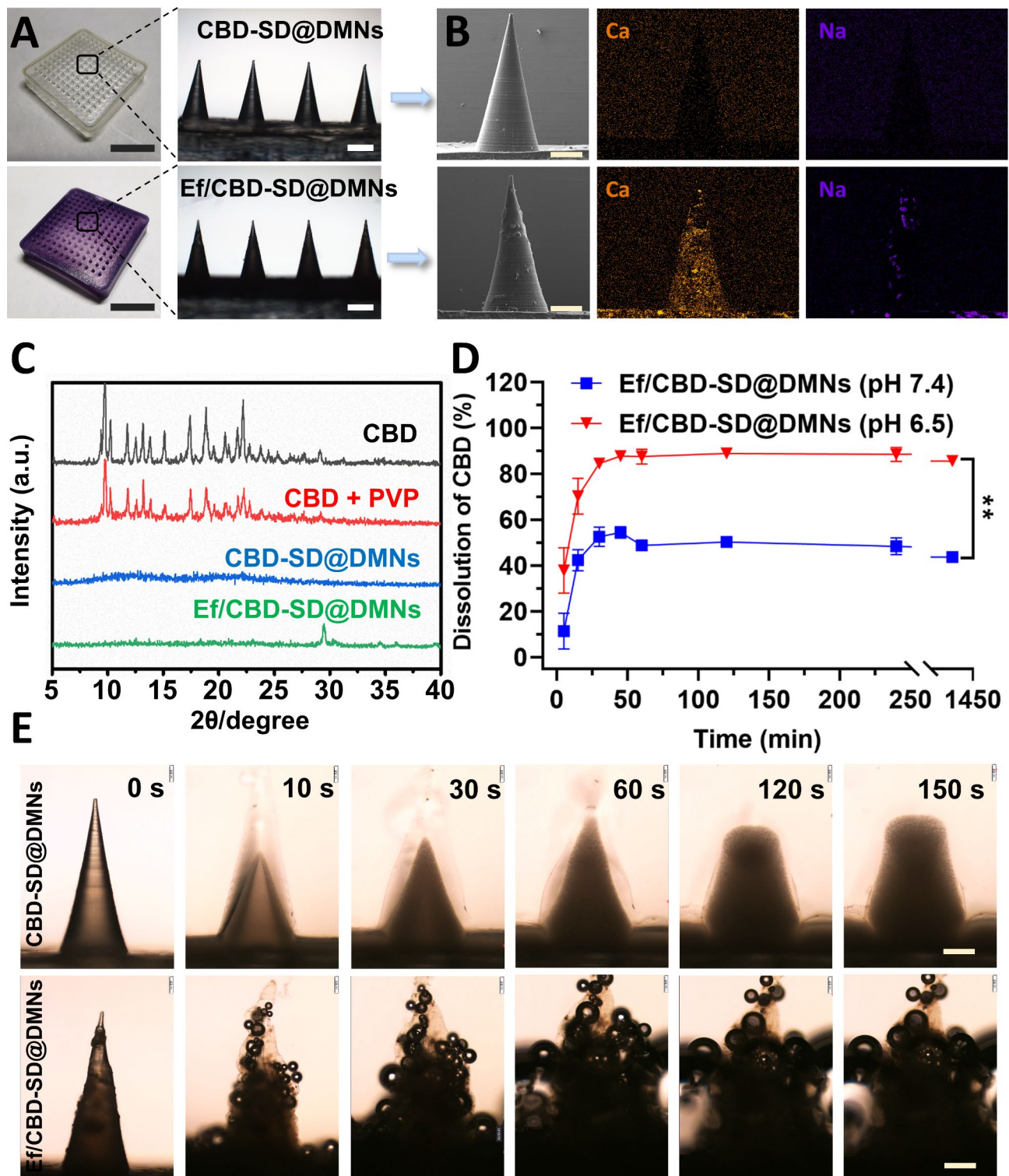


**Fig. 1** Preparation and characterizations of Ef/CBD-SD@DMNs. (A) Pictures of the patches (bar, 1 cm). The right part is the corresponding optical micrograph (bar, 500  $\mu\text{m}$ ). (B) SEM images and EDS analysis of CBD-SD@DMNs (upper) and Ef/CBD-SD@DMNs (lower). The bar is 250  $\mu\text{m}$ . (C) XRD spectrum of CBD-associated formulations. (D) Cumulative dissolution of CBD from Ef/CBD-SD@DMNs at different pH values. Data are represented as mean  $\pm$  SD,  $n=6$ . \*\* $P < 0.01$ . (E) CO<sub>2</sub> bubbles production and dissolution of the arrays in different pH environments within 150 s. The bar is 200  $\mu\text{m}$

content of CBD in the receiving cell and the cross-sectional area of the Franz diffusion cell, respectively.

Retention ( $\mu\text{g}/\text{cm}^2$ ) =  $C_r/S_F$ , where  $C_r$  and  $S_F$  are the

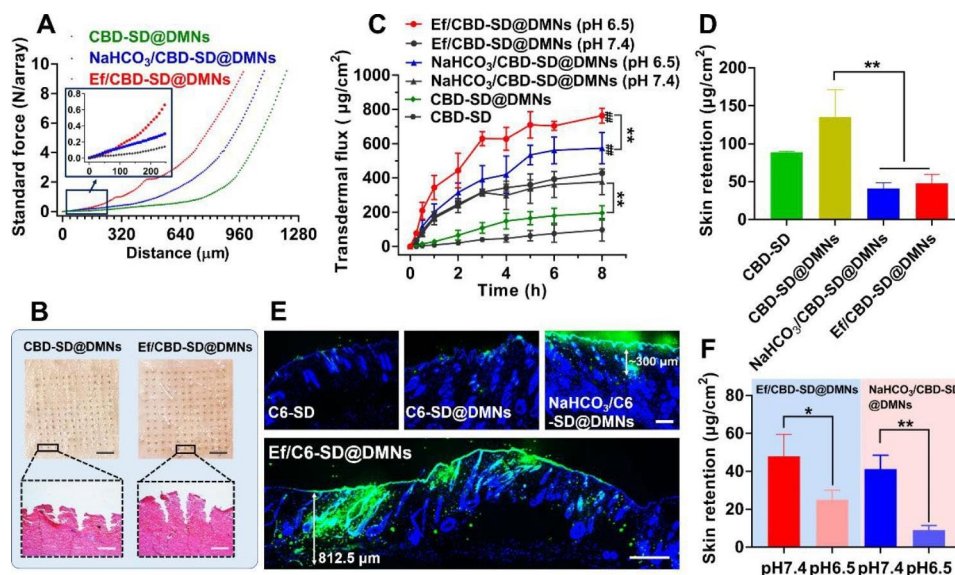


**Fig. 2** In vitro penetration and drug diffusion. (A) Force-distance curve of different CBD-SD@DMNs. (B) Images of porcine skins treated with different formulations and the H&E-stained sections. The bars are 2.5 mm (upper) and 200 μm (lower), respectively. (C) Dynamic transdermal flux of various formulations within 8 h. Data are represented as mean ± SD, n=6. \*\*\*P < 0.01; #P < 0.01 vs. the corresponding formulation at pH 7.4. (D) Skin retention of CBD after 8 h of treatments with different formulations. Data are represented as mean ± SD, n=6. \*\*\*P < 0.01. (E) Fluorescence images of various C6-labeled formulations-treated skins. The blue is DAPI and the green is the C6 signal. The bar is 200 μm (upper) and 450 μm (lower). (F) Skin retention of CBD after 8 h of treatments with the two effervescent DMNs at different pH values. Data are represented as mean ± SD, n=6. \*P < 0.05; \*\*P < 0.01

content of CBD in the skin and the cross-sectional area of the Franz diffusion cell, respectively.

### Cytotoxicity

Ten hundred thousand B16-F10 cells were seeded in the 96-well plates and cultured overnight. The groups set as follows, CBD (Ca<sup>2+</sup> (low)), CBD (Ca<sup>2+</sup> (medium)), and CBD (Ca<sup>2+</sup> (high)) at a CBD concentration ranging from 0–8 μg/mL. After being co-incubated for 24 h, the cells were stained with 10 μL of MTT (5 mg/mL) PBS solution for 4 h and dissolved with 150 μL DMSO. The absorbance in each well was determined at 450 nm with a microplate reader (MULTISKAN GO, Thermo Fisher, USA). The value of IC<sub>50</sub> was calculated by GraphPad Prism 8. Cell activity was calculated according to the following formula.

$$\text{Cell activity (\%)} = \frac{\text{OD}_{\text{Administration}} - \text{OD}_{\text{Blank}}}{\text{OD}_{\text{Control}} - \text{OD}_{\text{Blank}}} \times 100\%$$

Where OD<sub>Administration</sub>, OD<sub>Control</sub>, and OD<sub>Blank</sub> represent the absorbance of the administration group, control group, and blank group, respectively.

### Intracellular calcium determination

Five hundred thousand B16-F10 cells were seeded in the 6-well plates and cultured overnight. CBD (Ca<sup>2+</sup> (low)), CBD (Ca<sup>2+</sup> (medium)), and CBD (Ca<sup>2+</sup> (high)) at a CBD concentration of 2.5 μg/mL were co-incubated with the

cells for 2 h. And then, the cells were stained with Fluo-4 AM (1.5 μmol/L) in dark for 30 min, followed by washing with cold PBS and digesting with EDTA-free trypsin. The intracellular fluorescence was detected by a flow cytometer (Beckman Coulter, USA). Each experiment was done in triplicate.

### Apoptosis analysis

Five hundred thousand B16-F10 cells were seeded in the 6-well plates and cultured overnight. CBD (Ca<sup>2+</sup> (low)), CBD (Ca<sup>2+</sup> (medium)), and CBD (Ca<sup>2+</sup> (high)) at a CBD concentration of 2.5 μg/mL were co-incubated with the cells for 2 h. After being digested with EDTA-free trypsin, the cell suspension was stained with an appropriate volume of Annexin V-FITC and Propidium Iodide (KeyGEN, China) in dark for 10 min, followed by assaying using a flow cytometer (Beckman Coulter, USA) immediately. Each experiment was done in triplicate.

### Immunofluorescence staining in vitro

Five hundred thousand B16-F10 cells were seeded in the circle microscope cover glasses and cultured overnight. CBD (Ca<sup>2+</sup> (high)) at a CBD concentration of 0, 2.5, and 4 μg/mL were co-incubated with the cells for 2 h. After the removal of the medium, the cover glasses were fixed with 4% paraformaldehyde. Then, the cells were then permeabilized with Triton X-100 (0.1%, v%) for 15 min, followed by the addition of a blocking solution consisting of bovine serum albumin (BSA, 1%) and incubated at room temperature for 30 min. Next, all samples were incubated

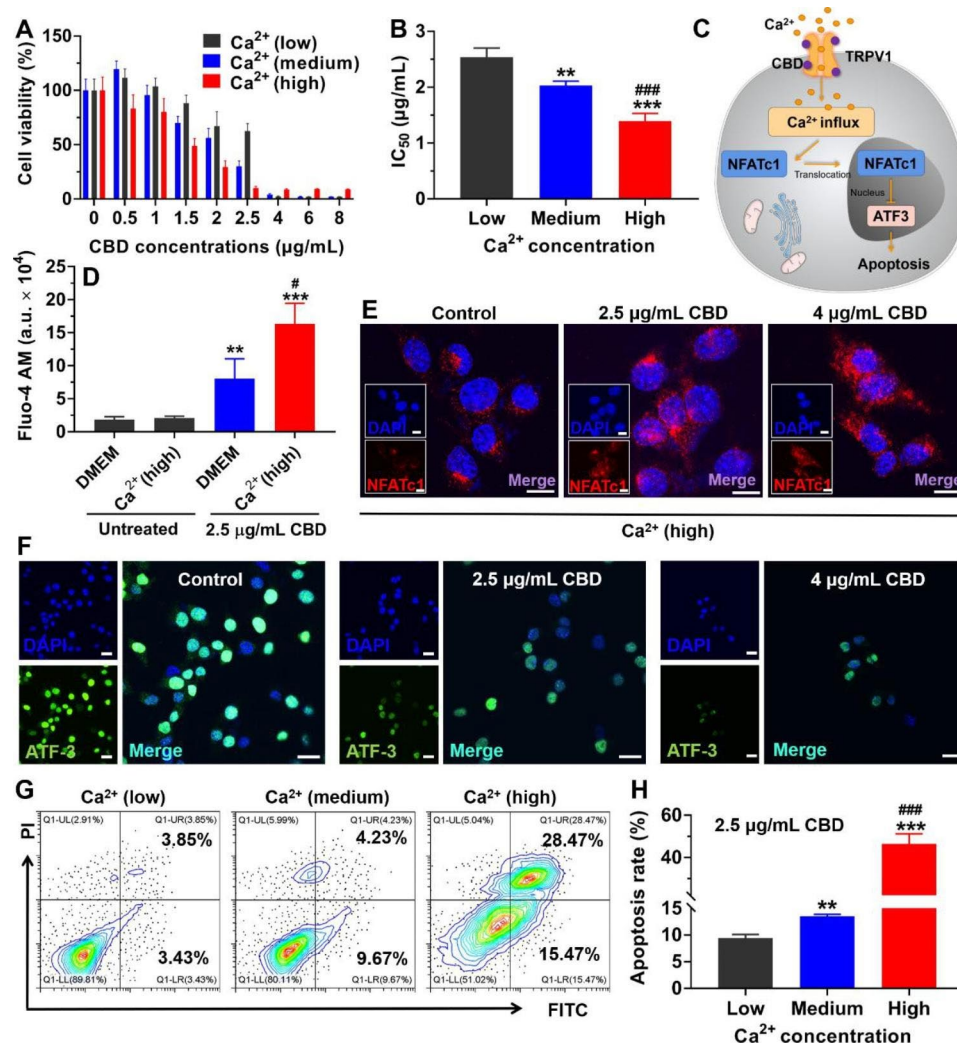


**Fig. 3** In vitro anti-melanoma mechanism. (A) B16-F10 cell viability and (B) the IC<sub>50</sub> after incubation with CBD-SD. Different concentrations of Ca<sup>2+</sup> were added in the culture medium. Data are represented as mean ± SD, n=4. \*\*P < 0.01. \*\*\*P < 0.001 vs. Low; ###P < 0.001 vs. Medium. (C) Schematic illustration of the "Ca<sup>2+</sup> influx-NFATc1-ATF3" pathway. (D) Fluorescence intensity of Fluo-4 AM in B16-F10 after different treatments. Data are represented as mean ± SD, n=4. \*\*P < 0.01. \*\*\*P < 0.001 vs. corresponding untreated group; #P < 0.05 vs. DMEM (2.5 µg/mL CBD). (E) Immunofluorescence staining of NFATc1 (red) of B16-F10 after different treatments. The bar is 10 µm. (F) Immunofluorescence staining of ATF3 (green) of B16-F10 after different treatments. The bar is 20 µm. (G) Representative flow cytometric and (H) quantitative analysis of apoptosis of B16-F10 cells after different treatments. Data are represented as mean ± SD, n=4. \*\*P < 0.01. \*\*\*P < 0.001 vs. Low; ###P < 0.001 vs. Medium

with the primary antibodies at room temperature for 12 h, followed by staining with the corresponding secondary antibodies in dark for 1 h. The primary antibodies included ATF3(ab207434, Abcam) and NFATc1(sc-7294, SANTA CRUZ). The following secondary antibodies included IgG (H+L) Fluor 555-conjugated (A0460, Beyotime) and IgG (H+L) Fluor 647-conjugated (A0468, Beyotime). Nuclei were labeled with DAPI (BL105A, Biosharp) at room temperature for 5 min. After washing with PBS thoroughly, immunofluorescence images were then acquired with a multiphoton confocal microscopy (STELLARIS 8 DIVE, Leica).

### Construction of B16-F10 xenograft-bearing mice

Two hundred microliters of B16-F10 cell suspension at a density of  $1 \times 10^4$  cells/µL was injected into the right back of C57BL/6J mice. The body weight and survival of mice were recorded daily. Tumor volume (mm<sup>3</sup>) was calculated according to the following formula,

$$\text{Tumor volume} = \frac{\text{length} \times \text{width}^2}{2}$$

Where length and width are the long diameter and short diameter of the tumor. Once the tumor size exceeded 50 mm<sup>3</sup>, transdermal therapy was performed.



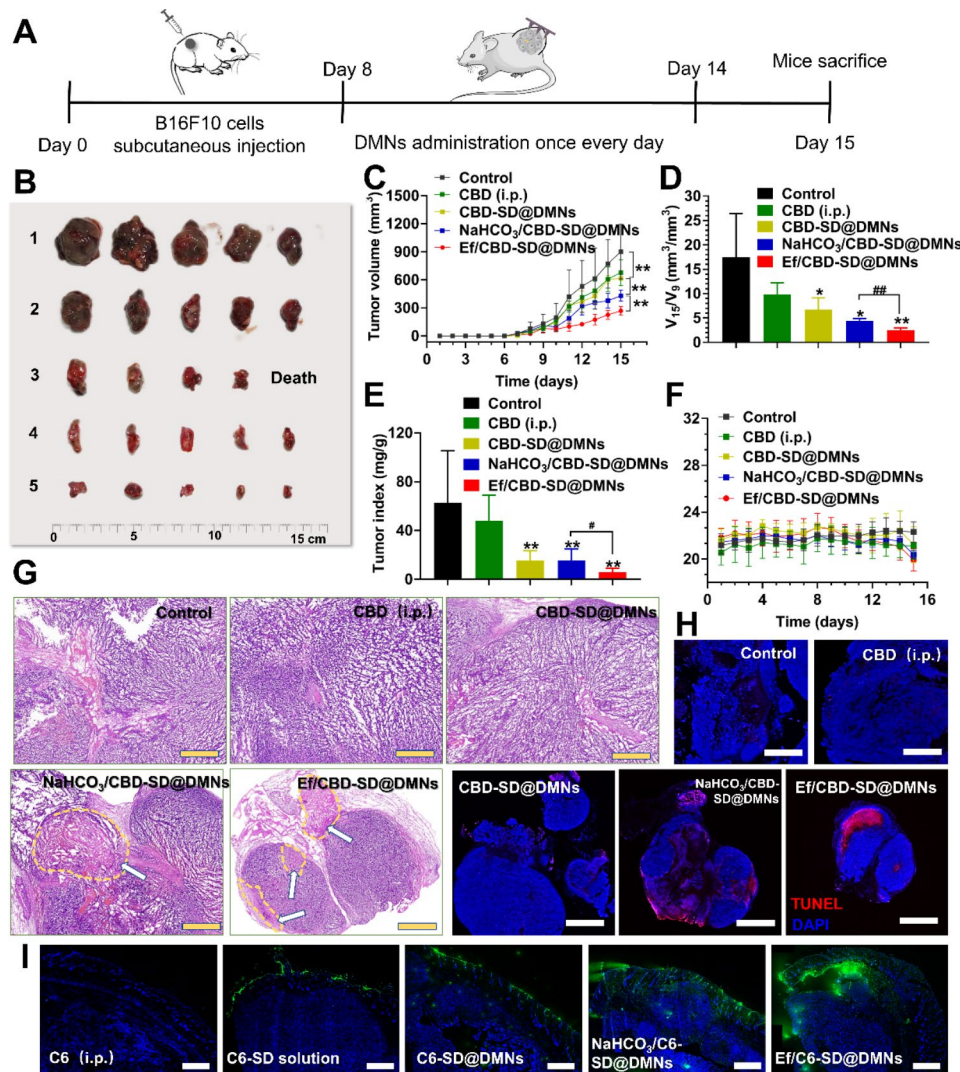


**Fig. 4** Anti-melanoma efficacy in vivo. (A) Schematic illustration of establishment of tumor-bearing mice model and therapeutic regimens. (B) Ex vivo tumors at the end of the treatments. (1. Control, 2. CBD (i.p.), 3. CBD-SD@DMNs, 4. NaHCO<sub>3</sub>/CBD-SD@DMNs, and 5. Ef/CBD-SD@DMNs.) (C) Tumor growth curve of mice treated with various treatments. Data are represented as mean  $\pm$  SD,  $n=5$ . \* $P < 0.05$ . \*\* $P < 0.01$ . \*\*\* $P < 0.001$ . (D) The ratio of tumor volume on day 15 to day 9. Data are represented as mean  $\pm$  SD,  $n=5$ . \* $P < 0.05$ . \*\* $P < 0.01$ . \*\*\* $P < 0.001$ . (E) Tumor index and (F) body weight of tumor-bearing mice treated with different treatments. Data are represented as mean  $\pm$  SD,  $n=5$ . \* $P < 0.05$ . \*\* $P < 0.01$ . \*\*\* $P < 0.001$ . (G) H&E-stained tumor sections after different treatments. The bar is 500  $\mu$ m. (H) Immunofluorescence staining of TUNEL of tumor sections after different treatments. The bar is 1 mm. (I) Fluorescence images of tumor sections of mice treated with various C6-labeled formulations. The bar is 2 mm

#### Antitumor Efficacy in vivo

The B16-F10 xenograft tumor-bearing mice were randomly divided into 5 groups ( $n=5$ ) as follows, control, CBD (i.p.), CBD-SD@DMNs, NaHCO<sub>3</sub>/CBD-SD@DMNs, and Ef/CBD-SD@DMNs. All the DMNs were administrated at a CBD dose of 5 mg/kg once every day. During the treatments, the body weight, tumor volume, and survival of the mice were recorded every day. After 7 days of the treatments, the mice were killed humanely, followed by harvesting the blood, tumors, hearts, livers, spleens, lungs, and kidneys. The tumor index (mg/g) was calculated according to the following formula. Tumor index =  $W_t/W_b$ , where  $W_t$  and  $W_b$

are the tumor weight and the body weight, respectively. To reflect the change in tumor volume before and after treatment,  $V_{15}/V_9$  ( $\text{mm}^3/\text{mm}^3$ ) was calculated, namely the ratio of tumor volume on day 15 to that on day 9. The serum was prepared to quantify inducible nitric oxide synthase (iNOS), interleukin-12P40 (IL-12P40), interleukin-6 (IL-6), interferon-gamma (IFN- $\gamma$ ), tumor necrosis factor- $\alpha$  (TNF- $\alpha$ ), interleukin-10 (IL-10), arginase 1 (Arg-1), and transforming growth factor- $\beta$ 1 (TGF- $\beta$ 1) using the corresponding ELISA kits under the manufacturer's protocol. Besides, the paraffin-embedded tumor sections were stained with H&E according to classic protocol.



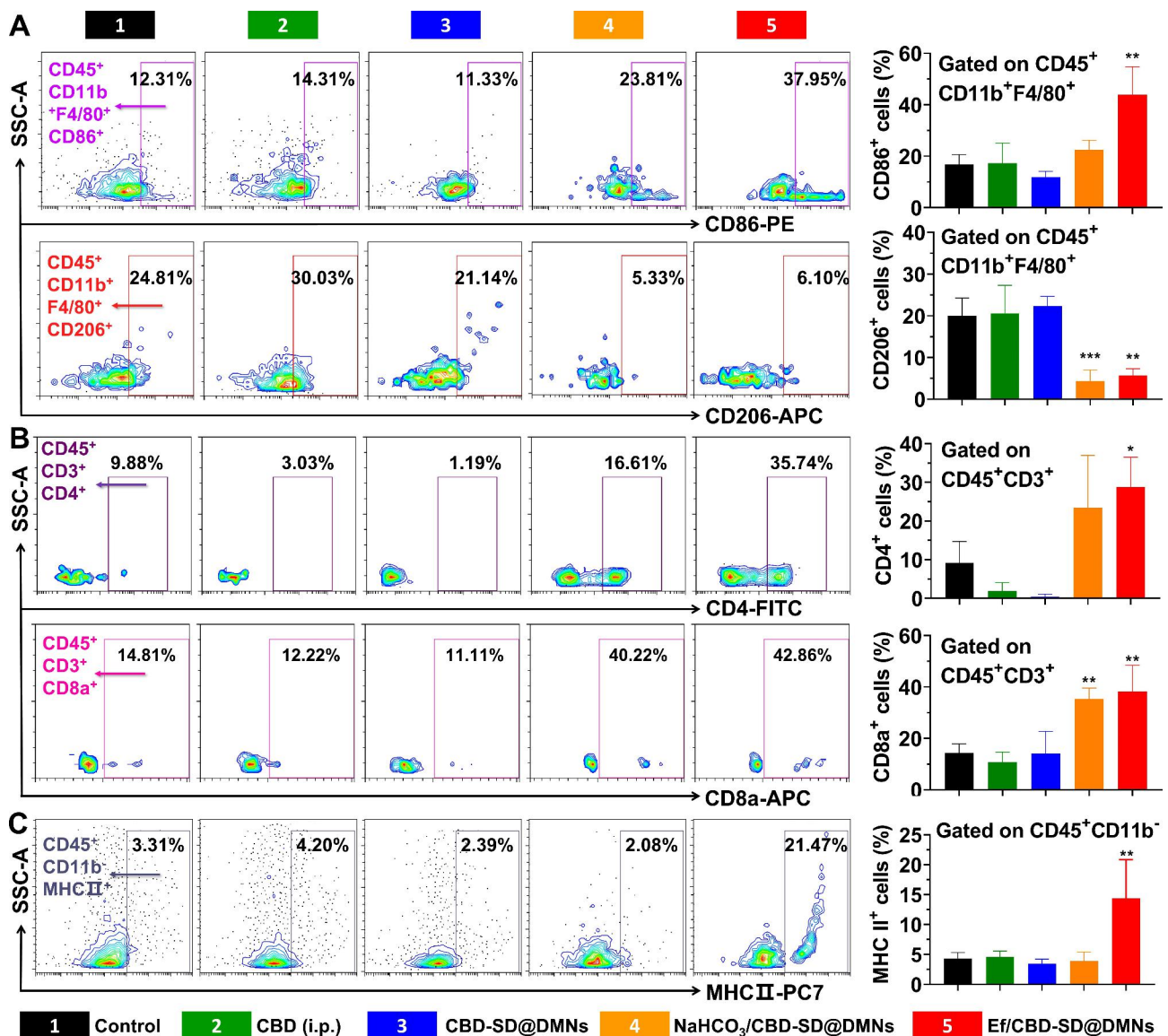


**Fig. 5** Influence on the tumoral immune cells. (A) Representative flow cytometric analysis and quantitative analysis of M1-like macrophages (CD86<sup>+</sup>) and M2-like macrophages (CD206<sup>+</sup>) gated on CD45<sup>+</sup>CD11b<sup>+</sup>F4/80<sup>+</sup> cells after different treatments. Data are represented as mean  $\pm$  SD,  $n=5$ . \*\* $P < 0.01$ . \*\*\* $P < 0.001$ . (B) Representative flow cytometric analysis and quantitative analysis of helper T cells (CD4<sup>+</sup>) and cytotoxic T cells (CD8<sup>+</sup>) gated on CD45<sup>+</sup>CD3<sup>+</sup> cells after different treatments. Data are represented as mean  $\pm$  SD,  $n=5$ . \* $P < 0.05$ . \*\* $P < 0.01$ . (C) Representative flow cytometric analysis and quantitative analysis of dendritic cell (MHC II<sup>+</sup>) gated on CD45<sup>+</sup>CD11b<sup>-</sup> cells after different treatments. Data are represented as mean  $\pm$  SD,  $n=5$ . \*\* $P < 0.01$

### Immune cells determination in tumors

The harvested tumors of the mice were cut into pieces in DMEM medium containing 2% FBS on ice and then treated with 5 volume equivalent trypsin at 37°C for 60 min. The samples were filtered and centrifuged at 600 g for 5 min. The cells were washed with PBS containing 2% FBS and co-incubated with sterile ZombieNIR dye and Fc receptor blocker at 4°C for 15 min. Next, the cells were stained with the primary antibodies in dark for 30 min, including anti-mouse CD86-PE antibody (B334834, Biolegend), anti-mouse CD206-APC (B354282, Biolegend), anti-mouse F4/80-PE/Cyanine-7

(B342137, Biolegend), anti-mouse CD45-Brilliant Violet 421 (B343559, Biolegend), anti-mouse CD3-PE (B341466, Biolegend), anti-mouse CD4-FITC (B269033, Biolegend), anti-mouse CD8a-APC (B348048, Biolegend), anti-mouse CD11c-APC (B339313, Biolegend), anti-mouse I-A/I-E (MHC II)-PE/Cyanine-7 (B337001, Biolegend) and anti-mouse CD11b-FITC (B349919, Biolegend). After rinsing excess antibodies, the cells were immediately assessed by a flow cytometer (Beckman Coulter, USA).

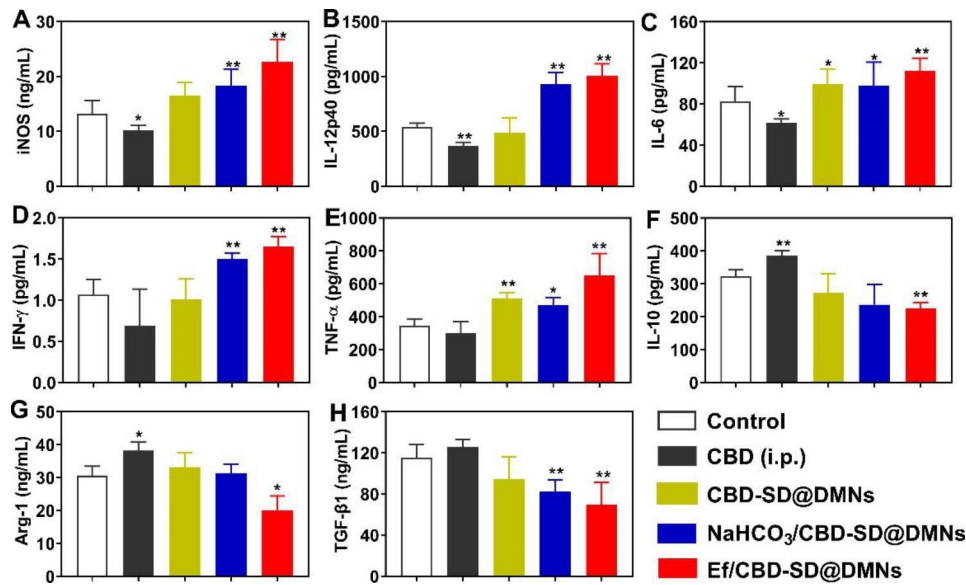


**Fig. 6** Serum cytokine detection. Changes in serum (A) iNOS, (B) IL-12p40, (C) IL-6, (D) IFN-γ, (E) TNF-α, (F) IL-10, (G) Arg-1, and (H) TGF-β1 after different treatments. Data are represented as mean ± SD, n = 5. \*P < 0.05. \*\*P < 0.01 vs. Control

**Immunofluorescence staining in vivo**

A part of the tumors from each group was successively deparaffinized, permeabilized, and blocked with 1% BSA as aforementioned. Next, all the samples were incubated

with primary antibodies at 37 °C for 1 h. The corresponding secondary antibodies were stained in dark for 1 h. The antibodies included TUNEL (ab66110, Abcam), ATF3(ab207434, Abcam), NFATc1(sc-7294, SANTA

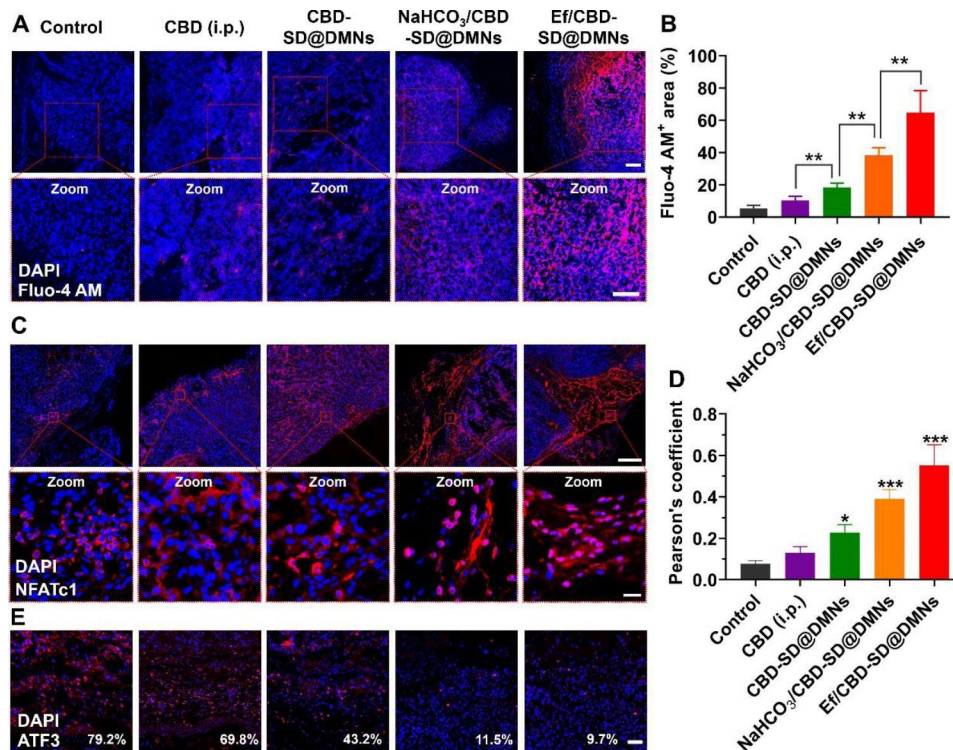


**Fig. 7** Validation of Ca<sup>2+</sup> influx-NFATc1-ATF3 signaling inside the tumors. (A) Immunofluorescence staining and (B) quantitative analysis of Fluo-4 AM in the tumors after different treatments. The bar is 100 μm. Data are represented as mean ± SD, n = 5. \*\*P < 0.01. (C) Immunofluorescence staining and (D) quantitative analysis of NFATc1 in the tumors after different treatments. The bar is 400 μm (upper) and 40 μm (lower). Data are represented as mean ± SD, n = 5. \*P < 0.05; \*\*\*P < 0.001 vs. Control. (E) Immunofluorescence staining of ATF3 in the tumors after different treatments. The bar is 50 μm

CRUZ), and Foxp3-PE (B325779, Biolegend). Nuclei were labeled with DAPI for 5 min. After washing with PBS thoroughly, the fluorescent images were acquired with a CLSM (FV101i, OLYMPUS) and quantified by Image J software.

### Transdermal and tumoral penetration

The B16-F10 xenograft tumor-bearing mice were randomly divided into 5 groups as follows, C6 (i.p.), C6 solution, C6-SD@DMNs, NaHCO<sub>3</sub>/C6-SD@DMNs, and Ef/C6-SD@DMNs. Each group of mice was administrated at a C6 dosage of 5 mg/kg and killed humanely after 1 h. Each tumor was collected and prepared into frozen sections. The nuclei were labeled with DAPI for 5 min. After the removal of excess dyes, the tumor sections were fixed with 4% paraformaldehyde, sealed with an anti-fade mounting medium, and immediately observed by a CLSM (FV101i, OLYMPUS).

### Skin irritation

The right-back skin of male C57BL/6J mice was depilated and disinfected. Then the microneedles were pressed to the skin for 5 min once every day for 7 days. The surface of the treated skin was observed daily.

### Data analysis

All Data presented in this study were shown as a mean ± standard deviation (SD). Statistical tests were performed by GraphPad prism 8.0 statistical software. ANOVA was employed to evaluate the statistical significance. Statistical significance was defined as the values of \*P < 0.05, \*\*P < 0.01, and \*\*\*P < 0.001.

## Results

### Fabrication and characterizations of Ef/CBD-SD@DMNs

Ef/CBD-SD@DMNs were facilely fabricated by the “one-step micro-molding” method, as presented in Scheme 1A. As shown in Fig. 1A, the CBD-SD@DMNs transparent patch had 12 × 12 uniform conical arrays with a base diameter of ~460 μm and a height of ~1000 μm. The morphology and corresponding energy dispersive X-ray spectroscopy (EDS) mapping analysis of Ef/CBD-SD@DMNs exhibited a uniform dispersion of NaHCO<sub>3</sub> and CaCO<sub>3</sub> in the array (Fig. 1B), which resulted in a slightly-rough surface in comparison with that of CBD-SD@DMNs. According to the X-ray diffraction (XRD) of Ef/CBD-SD@DMNs, the characteristic diffractive peaks ascribed to both CBD and PVP disappeared (Fig. 1C). Due to the SD and effervescent design, cumulative dissolution of CBD from Ef/CBD-SD@DMNs reached ~90% within 30 min in a mildly-acidic environment, which was 1.73 times that in the physiological environment (Fig. 1D). In contrast, due to the lack of the effervescent components, the 24 h-cumulative dissolution rate of

CBD-SD@DMNs was about 50%, which is not dependent on the pH environment (Figure S1). As shown in Fig. 1E, Ef/CBD-SD@DMNs produced plenty of bubbles in PBS (pH 6.5) within 60 s (Fig. 1E).

### Penetration and transdermal delivery in vitro

As shown in Fig. 2A, the insertion force of the three SD@DMNs reached at least 10 N/array, and Ef/CBD-SD@DMNs exhibited the strongest hardness. As illustrated in the HE-stained images (Fig. 2B), Ef/CBD-SD@DMNs successfully pierced the pig skin and reached the epidermis (>700 μm), which is deeper than CBD-SD@DMNs. In addition, Ef/CBD-SD@DMNs were able to pierce the three-layer parafilm, with a significantly higher penetration rate than CBD-SD@DMNs (Figure S2). To investigate the transdermal performance of Ef/CBD-SD@DMNs, fluorescence distribution and drug quantification in the porcine skin were studied, respectively. As demonstrated in Fig. 2C, the 8 h-cumulative transdermal flux of CBD-SD@DMNs was ~120 μg/cm<sup>2</sup>, significantly higher than that of CBD-SD. Similarly, the dynamic transdermal flux of NaHCO<sub>3</sub>/CBD-SD@DMNs at pH 7.4 was significantly improved compared to that of CBD-SD@DMNs. Notably, the transdermal flux of NaHCO<sub>3</sub>/CBD-SD@DMNs and Ef/CBD-SD@DMNs at pH 6.5 was noticeably improved in comparison to their behavior at pH 7.4. The 8 h-cumulative transdermal flux of Ef/CBD-SD@DMNs reached ~710 μg/cm<sup>2</sup>, remarkably higher than that of NaHCO<sub>3</sub>/CBD-SD@DMNs. However, no statistical difference in transdermal behavior was observed between NaHCO<sub>3</sub>/CBD-SD@DMNs and Ef/CBD-SD@DMNs at pH 7.4. Undesired retention in the skin is not favorable to the transdermal delivery, nor is it for tumoral penetration. As shown in Fig. 2D, the 8 h-cumulative skin retention of CBD-SD@DMNs at pH 7.4 was ~130 μg/cm<sup>2</sup>, which is significantly higher than that of both NaHCO<sub>3</sub>/CBD-SD@DMNs and Ef/CBD-SD@DMNs. The skin retention of the two effervescent DMNs considerably decreased at pH 6.5 than that at pH 7.4 (Fig. 2F). In addition, after pressing Ef/C6-SD@DMNs into the skin, the C6 signal was observed at a distance of ~812.5 μm from the stratum corneum, which is notably deeper than the NaHCO<sub>3</sub>/C6-SD@DMNs (only ~300 μm), as well as the C6-SD@DMNs. These findings further indicate that the effervescent components generating CO<sub>2</sub> bubbles actively push the drug towards efficient transdermal delivery. Moreover, considering possible skin irritation, the safety of Ef/CBD-SD@DMNs was evaluated. As shown in Figure S3, Ef/CBD-SD@DMNs inserted into the skin once every day for 7 days did not cause any wounds.



### Efficacy and mechanism of anti-melanoma in vitro

To figure out whether the incorporation of  $\text{CaCO}_3$  into Ef/CBD-SD@DMNs could enhance the anti-melanoma effect, the inhibition of CBD-SD against B16-F10 cells cultured with different calcium concentrations was investigated. As shown in Fig. 3A and B, treatment with CBD-SD significantly suppressed the viability of B16-F10 cells cultured with high calcium concentrations once the CBD concentration exceeded  $1.5 \mu\text{g/mL}$ , with an  $\text{IC}_{50}$  of  $\sim 2.03 \mu\text{g/mL}$ , which is significantly lower than that of the medium- and low-calcium groups. As reported previously [3], increased calcium influx triggered the nuclear translocation of NFATc1, subsequently downregulated the transcription factor ATF3, and consequently led to melanoma apoptosis (Fig. 3C). To elucidate the anti-melanoma mechanism of the CBD-SD and calcium ions, the “TRPV1-NFATc1-ATF3” pathway was studied under different calcium concentrations. As shown in Fig. 3D, the intracellular Fluo-4 AM fluorescence had no significant change regardless of whether B16-F10 cells were cultured with the normal DMEM medium or supplemented with exogenous calcium ions. In contrast, after the treatment with CBD-SD at a CBD concentration of  $2.5 \mu\text{g/mL}$ ,  $\text{Ca}^{2+}$  influx noticeably enhanced with the exogenous calcium increased (Fig. 3D). The NFATc1 was distributed in the cytoplasm of the untreated B16-F10 cells. Once treated with CBD-SD, the nuclear translocation of NFATc1 presenting as the overlap of the red and blue signal was easily observed (Fig. 3E). Under the high-calcium conditions, the expression of ATF3 in the nucleus was significantly reduced with the treatment of CBD-SD (Fig. 3F). As demonstrated in Fig. 3G H, high-calcium culture conditions significantly improved the apoptosis-inducing effect of CBD-SD on B16-F10 cells.

### Anti-melanoma efficacy in vivo

After the establishment of the B16-F10 melanoma-bearing mice model, various DMNs were administrated at a CBD dosage of  $5 \text{ mg/kg}$  once every day for 7 days (Fig. 4A). As a control, the mice were intraperitoneally injected with CBD (CBD (i.p.),  $5 \text{ mg/kg}$ ) once every two days [41]. As shown in Fig. 4B, the treatment of CBD (i.p.) slightly inhibited the growth of melanoma, while the volume of the tumors of mice treated with the three DMNs was significantly shrunk compared to the control group. According to the tumor growth curve (Fig. 4C), the average volume of tumors of mice treated with  $\text{NaHCO}_3/\text{CBD-SD@DMNs}$  was remarkably smaller than that of CBD-SD@DMNs. Ef/CBD-SD@DMNs exhibited the most significant inhibition against melanoma among all the groups. The  $V_{15}/V_9$ , representing the growth rate of melanoma, was noticeably retarded after the treatment with the three DMNs. As expected, Ef/CBD-SD@DMNs presented a significantly lower  $V_{15}/V_9$

than  $\text{NaHCO}_3/\text{CBD-SD@DMNs}$  (Fig. 4D). Besides, the treatment with Ef/CBD-SD@DMNs resulted in the lowest tumor index among all the groups (Fig. 4E). The body weight of the mice treated with different formulations showed no significant fluctuation (Fig. 4F), indicating acceptable systemic safety. According to the HE-stained and TUNEL-stained tumor sections, the two effervescent CBD-SD@DMNs groups not only resulted in obvious necrosis but also induced substantial tumor cell apoptosis (Fig. 4G H). According to our hypothesis, effervescent DMNs improve anti-melanoma efficacy by  $\text{CO}_2$  bubbles-thrusted transdermal and tumoral penetration. As shown in Fig. 4I, the penetration of the two effervescent DMNs was notably deeper than that of CBD-SD@DMNs. After treatment with Ef/C6-SD@DMNs, intratumoral C6 distribution was obviously higher than  $\text{NaHCO}_3/\text{C6-SD@DMNs}$ .

### Engineering of the TME

As shown in Fig. 5A, neither CBD (i.p.) nor CBD-SD@DMNs treatment influenced the population of  $\text{CD45}^+\text{CD11b}^+\text{F4/80}^+\text{CD86}^+$  or  $\text{CD45}^+\text{CD11b}^+\text{F4/80}^+\text{CD206}^+$  cells, which are ascribed to the M1 and M2 TAMs, respectively [42]. Notably, Ef/CBD-SD@DMNs could not only increase M1 TAMs but also decrease M2 TAMs in the TME. Likewise,  $\text{NaHCO}_3/\text{CBD-SD@DMNs}$  could also decrease the percentage of M2 TAMs. Such similar  $\text{H}^+$  elimination-resulted TAMs repolarization is in accordance with a previous report [38]. Likewise, the treatment with Ef/CBD-SD@DMNs led to a higher population of  $\text{CD45}^+\text{CD3}^+\text{CD4}^+$ , as well as  $\text{CD45}^+\text{CD3}^+\text{CD8}^+$  cells; however, the CBD-SD@DMNs did not change the percentage of  $\text{CD45}^+\text{CD3}^+\text{CD4}^+$  or  $\text{CD45}^+\text{CD3}^+\text{CD8}^+$  cells (Fig. 5B), indicating that effervescent component is a potential reason for enhanced infiltration of T cells. Besides, Ef/CBD-SD@DMNs was even able to reduce the abundance of regulatory T cells (Foxp3<sup>+</sup> area) in the TME (Figure S4). The percentage of T cells in the spleen was not changed noticeably after treatments with different DMNs (Figure S5). Although the recruitment of DCs precursors from peripheral circulation into certain tissues is dependent on  $\text{Ca}^{2+}$  signaling [43], whether sufficient  $\text{Ca}^{2+}$  influx can increase the abundance of intratumoral mature DCs remains unclear. As displayed in Fig. 5C, Ef/CBD-SD@DMNs significantly increased the abundance of  $\text{CD45}^+\text{CD11b}^-\text{MHC II}^+$  cells but  $\text{NaHCO}_3/\text{CBD-SD@DMNs}$  failed, suggesting that the introduction of exogenous calcium to the tumors also increases DCs in the TME.

As shown in Fig. 6A~6 C, the serum iNOS, IL-12p40, and IL-6 (considered Th1 cytokines) of mice treated with CBD (i.p.) were decreased significantly compared with the control group, which might be associated

with the anti-inflammatory effects of CBD. In contrast, NaHCO<sub>3</sub>/CBD-SD@DMNs and Ef/CBD-SD@DMNs upregulated the level of iNOS, IL-12p40, IL-6, IFN- $\gamma$ , and TNF- $\alpha$ , which could trigger pro-inflammatory effects and consequently activate the TME (Fig. 6A~6E). Moreover, Ef/CBD-SD@DMNs also downregulated serum levels of IL-10, Arg-1, and TGF- $\beta$ 1 (Fig. 6F~6H), which can alleviate immunosuppression.

#### Ca<sup>2+</sup> influx-NFATc1-ATF3 signaling in vivo

As shown in Fig. 7A and B, CBD-SD@DMNs significantly increased Ca<sup>2+</sup> influx in the tumor compared to the CBD (i.p.) group. The NaHCO<sub>3</sub>/CBD-SD@DMNs group exhibited remarkably higher Fluo-4 AM fluorescence than the CBD-SD@DMNs group, and mice treated with Ef/CBD-SD@DMNs had red fluorescence distributed almost throughout the tumor section, possibly due to calcium carbonate in the effervescent components. Immunofluorescent staining revealed nuclear translocation of NFATc1 triggered by Ca<sup>2+</sup> influx (Fig. 7C and D). The NFATc1 was almost completely transferred into the nucleus in the Ef/CBD-SD@DMNs group, where the Pearson's coefficient of the two fluorescence reached ~0.6, significantly higher than the NaHCO<sub>3</sub>/CBD-SD@DMNs and CBD-SD@DMNs group. According to the trend, the nucleus translocation of the NFATc1 is related to the amount of intracellular CBD. Afterward, the expression of ATF3 inside the tumors of mice treated with different formulations was investigated. As shown in Fig. 7E, the ATF3-positive area of tumor sections in the two effervescent CBD-SD@DMNs was significantly lower than that in the CBD-SD@DMNs group.

#### Discussion

In this study, we successfully fabricated Ef/CBD-SD@DMNs using a one-step micro-molding method. To ensure a good dispersibility and hardness, PVP was employed as the matrix of both SD and DMNs, while the effervescent design significantly improved the dissolution of Ef/CBD-SD@DMNs in mildly-acidic environments through producing CO<sub>2</sub> bubbles, which may increase the penetration of CBD into tumors. The addition of effervescent ingredients resulted in a slightly-rough surface and a purple color change, probably due to the color reaction of CBD in the weak base environment. XRD analysis indicated that the CBD in Ef/CBD-SD@DMNs was probably in an amorphous form, which has better dissolution and desired internalization, potentially improving the bioavailability of CBD. Adequate stiffness is a prerequisite for microneedles to penetrate the skin. In our research, the insertion force of the three SD@DMNs surpassed the threshold (0.098 N/needle) required for piercing the stratum corneum [28]. The introduction of combined effervescent ingredients in Ef/CBD-SD@

DMNs resulted in stronger mechanical properties compared to NaHCO<sub>3</sub>/CBD-SD@DMNs, leading to deeper skin penetration. In addition, the effervescent components significantly promoted transdermal delivery in both physiological and acidic environments. This is probably because the effervescent components rapidly generate CO<sub>2</sub> bubbles and actively push the drug deep into the skin. In general, the improved transdermal delivery of Ef/CBD-SD@DMNs can be attributed to the stronger array rigidity and rapid gas generation, which can effectively "blow" the CBD into the deeper layers of the skin.

As described in the introduction section, the downregulation of TRPV expression can inhibit the development of melanoma by increasing the Ca<sup>2+</sup> influx. In vitro studies have demonstrated that CBD-SD induces B16-F10 cell apoptosis via the "TRPV1-NFATc1-ATF3" pathway. Specifically, increased calcium influx triggered the nuclear translocation of NFATc1, which subsequently downregulated the transcription factor ATF3, leading to melanoma apoptosis. These findings provide insights into the molecular mechanisms underlying the anti-melanoma effect of CBD-SD. Furthermore, sufficient calcium ions are of great importance for CBD to initiate calcium influx, the incorporation of CaCO<sub>3</sub> provides sufficient calcium for Ca<sup>2+</sup> influx, underscoring the importance of our Ef/CBD-SD@DMNs design from the aspect of combinational melanoma therapy.

In vivo, the anti-melanoma efficacy of Ef/CBD-SD@DMNs was found to be the most significant among all the treatment groups. Our research confirmed that intratumoral CBD increases Ca<sup>2+</sup> influx, transfers NFATc1 into the nucleus, and then downregulates ATF3 expression, ultimately inducing melanoma cell apoptosis, which validate our aforementioned hypothesis regarding the anti-melanoma efficacy and in vivo mechanisms. Successful intervention in this pathway depends on transdermal delivery and tumoral penetration of CBD. The rationale for incorporating CaCO<sub>3</sub> into Ef/CBD-SD@DMNs was further verified from both the perspectives of anti-melanoma efficacy and transdermal drug delivery.

In a previous report, it was suggested that glycolytic metabolism within the tumor microenvironment can result in the overproduction of lactic acid and decrease in intra-tumoral pH. This creates a hypoxic environment and disrupts the energy metabolism balance, ultimately leading to the suppression of the TME [44]. The results of this study suggest that Ef/CBD-SD@DMNs can promote M1 repolarization of TAMs and reduce the abundance of immunosuppressive cells, such as M2 TAMs and regulatory T cells, ultimately leading to the activation of the entire TME. This response could be attributed to the elimination of H<sup>+</sup> within the tumor via effervescence and the introduction of exogenous calcium, which positively modulates the TME towards an anti-tumoral response.

However, there are several issues that need to be clarified in this study. Firstly, the specific molecular mechanisms underlying the clearing of the intra-tumoral proton-regulated microenvironment remain unclear. So far, no direct evidence has yet confirmed whether the polarization of M1 TAMs or enhanced calcium ions influx leads to the activation of the TME. Secondly, the direction of gas production in this study is random and lacks sufficient targeting ability, although it can enhance transdermal drug delivery. Additionally, the biodistribution of Ef/CBD-SD@DMNs following transdermal administration remains undetermined. Thus, it is currently unknown how much CBD directly enters the tumor via transdermal delivery and how much is distributed via the blood circulation. These issues will be addressed in future studies to further improve the understanding of the mechanisms underlying Ef/CBD-SD@DMNs action.

## Conclusion

In summary, the novel Ef/CBD-SD@DMNs system developed in this study offers a promising approach to improve the efficacy of CBD-based therapy for melanoma. Ef/CBD-SD@DMNs combines the advantages of effervescence and CBD-based solid dispersion to achieve better transdermal and tumoral delivery of CBD. The *in vitro* and *in vivo* results demonstrate that Ef/CBD-SD@DMNs can not only effectively induce melanoma apoptosis via the “Ca<sup>2+</sup> influx-NFATc1-ATF3” pathway but also activate the tumor microenvironment probably through increasing intra-tumoral pH environment. This study provides a facile and efficient design for a transdermal delivery system that may have a significant impact on the development of new melanoma therapies.

## Abbreviations

CBD	Cannabidiol
DMNs	Dissolving microneedles
CBD-SD	CBD-based solid dispersion
CBD-SD@DMNs	Cannabidiol solid dispersion-doped dissolving microneedles
NaHCO <sub>3</sub> /CBD-SD@DMNs	Cannabidiol solid dispersion-doped dissolving microneedles with NaHCO <sub>3</sub>
Ef/CBD-SD@DMNs	Effervescent cannabidiol solid dispersion-doped dissolving microneedles
TRPV1	Transient receptor potential vanilloid 1
NFATc1	Nuclear factor of activated T-Cells, cytoplasmic 1
ATF3	Activating transcription factor 3
TME	Tumor microenvironment
TAMs	Tumor-associated macrophages
PVP	Polyvinyl pyrrolidone
SEM	Scanning electron microscope
EDS	Energy dispersive X-ray spectroscopy
XRD	X-ray diffraction
CLSM	Confocal laser scanning microscopy
C6	Coumarin 6
DAPI	4,6-diamidino-2-phenylindole

## Supplementary Information

The online version contains supplementary material available at <https://doi.org/10.1186/s40824-023-00390-x>.

Supplementary Material 1

Supplementary Material 2

Supplementary Material 3

## Acknowledgements

Not applicable.

## Author Contribution

Q D and S J C designed the experiments. S J C and M Q L carried out the fabrication and characterizations of Ef/CBD-SD@DMNs and penetration and transdermal delivery *in vitro*. S J C, M Q L, S W T, and K F carried out the efficacy and mechanism of anti-melanoma *in vitro*. S J C, M Q L, S W T, G C, Q D, and J X carried out the anti-melanoma efficacy *in vivo*, engineering of the TME and Ca<sup>2+</sup> influx-NFATc1-ATF3 signaling *in vivo*. S J C, M Q L, and Q D performed data analysis. S J C and Q D wrote the manuscript. Q D, S J C, M Q L, L C Y, L Y P, Z H Q, L X Q, and C Y revised the manuscript. All the authors have read and approved the final manuscript.

## Funding

This work was supported by the National Natural Science Foundation of China (82173980 and 81873017), the Natural Science Foundation of Jiangsu Province of China (BK20211389 and BK20210694), General Project of Jiangsu Provincial Health Commission (M2021010), the Open Project of Chinese Materia Medica First-Class Discipline of Nanjing University of Chinese Medicine (2020YLXK015), the Six Talent Peak Project of Jiangsu Province (YY-028-2019), and “333 project” of Jiangsu Province.

## Data Availability

All data presented in this paper are included in the main text and the supplementary information.

## Declarations

### Ethics approval and consent to participate

All animals were treated in accordance with the Guide for Care and Use of Laboratory Animals published by the Animal Ethic Committee of Nanjing University of Chinese Medicine.

### Consent for publication

All authors of this study agreed to publish.

### Competing interests

No potential conflict of interest was reported by the authors.

### Author details

<sup>1</sup>Affiliated Hospital of Integrated Traditional Chinese and Western Medicine, Nanjing University of Chinese Medicine, Nanjing 210028, China  
<sup>2</sup>Jiangsu Province Academy of Traditional Chinese Medicine, Nanjing 210028, China

Received: 2 February 2023 / Accepted: 7 May 2023

Published online: 18 May 2023

## References

- Arnold M, Singh D, Laversanne M, Vignat J, Vaccarella S, Meheus F, et al. Global burden of cutaneous melanoma in 2020 and projections to 2040. *JAMA dermatology*. 2022;158(5):495–503.
- Skudalski L, Waldman R, Kerr PE, Grant-Kels JM. Melanoma: an update on systemic therapies. *J Am Acad Dermatol*. 2022;86(3):515–24.



3. Yang Y, Guo W, Ma J, Xu P, Zhang W, Guo S, et al. Downregulated TRPV1 expression contributes to Melanoma Growth via the Calcineurin-ATF3-p53 pathway. *J Invest Dermatol*. 2018;138(10):2205–15.
4. Nam JH, Nam DY, Lee DU. Valencene from the Rhizomes of *Cyperus rotundus* inhibits skin photoaging-related Ion Channels and UV-Induced Melanogenesis in B16F10 Melanoma cells. *J Nat Prod*. 2016;79(4):1091–6.
5. Zheng J, Liu F, Du S, Li M, Wu T, Tan X, et al. Mechanism for regulation of Melanoma Cell Death via activation of Thermo-TRPV4 and TRPV2. *J Oncol*. 2019;2019:7362875.
6. Chen J, Luan Y, Yu R, Zhang Z, Zhang J, Wang W. Transient receptor potential (TRP) channels, promising potential diagnostic and therapeutic tools for cancer. *Biosci Trends*. 2014;8(1):1–10.
7. Zhong T, Zhang W, Guo H, Pan X, Chen X, He Q, et al. The regulatory and modulatory roles of TRP family channels in malignant tumors and relevant therapeutic strategies. *Acta Pharm Sin B*. 2022;12(4):1761–80.
8. Tijani AO, Thakur D, Mishra D, Frempong D, Chukwunyeri UI, Puri A. Delivering therapeutic cannabinoids via skin: current state and future perspectives. *J Control Release*. 2021;334:427–51.
9. Phatale V, Vaiphei KK, Jha S, Patil D, Agrawal M, Alexander A. Overcoming skin barriers through advanced transdermal drug delivery approaches. *J Control Release*. 2022;351:361–80.
10. Yang Y, Zhou R, Wang Y, Zhang Y, Yu J, Gu Z. Recent advances in oral and transdermal protein Delivery Systems. *Angew Chem*. 2023;62(10):e202214795.
11. Nguyen TT, Nguyen TTD, Tran NM, Vo GV. Advances of microneedles in hormone delivery. *Biomed Pharmacother*. 2022;145:112393.
12. Li Y, He G, Fu LH, Younis MR, He T, Chen Y, et al. A Microneedle Patch with Self-Oxygenation and glutathione depletion for repeatable photodynamic therapy. *ACS Nano*. 2022;16(10):17298–312.
13. Joo SH, Kim J, Hong J, Fakhraei Lahiji S, Kim YH. Dissolvable self-locking Microneedle Patches Integrated with Immunomodulators for Cancer Immunotherapy. *Adv Mater*. 2023;35(10):e2209966.
14. Chen J, Niu H, Guan L, Yang Z, He Y, Zhao J, et al. Microneedle-Assisted transdermal delivery of 2D Bimetallic Metal-Organic Framework Nanosheet-Based Cascade Biocatalysts for enhanced Catalytic Therapy of Melanoma. *Adv Healthc Mater*. 2022;12(7):e2202474.
15. Wang H, Fu Y, Mao J, Jiang H, Du S, Liu P, et al. Strong and tough Supramolecular Microneedle Patches with Ultrafast Dissolution and Rapid-onset capabilities. *Adv Mater*. 2022;34(51):e2207832.
16. Ingrole RSJ, Gill HS. Microneedle Coating Methods: a review with a perspective. *J Pharmacol Exp Ther*. 2019;370(3):555–69.
17. Abd-El-Azim H, Tekko IA, Ali A, Ramadan A, Nafee N, Khalafallah N, et al. Hollow microneedle assisted intradermal delivery of hypericin lipid nanocapsules with light enabled photodynamic therapy against skin cancer. *J Control Release*. 2022;348:849–69.
18. Narayanan SP, Raghavan S. Solid silicon microneedles for drug delivery applications. *Int J Adv Manuf Tech*. 2017;93(1–4):407–22.
19. Sartawi Z, Blackshields C, Faisal W. Dissolving microneedles: applications and growing therapeutic potential. *J Control Release*. 2022;348:186–205.
20. Lee H, Song C, Baik S, Kim D, Hyeon T, Kim DH. Device-assisted transdermal drug delivery. *Adv Drug Deliv Rev*. 2018;127:35–45.
21. Jennotte O, Koch N, Lechanteur A, Evrard B. Development of amorphous solid dispersions of cannabidiol: Influence of the carrier, the hot-melt extrusion parameters and the use of a crystallization inhibitor. *J Drug Deliv Sci Technol*. 2022;71.
22. Grifoni L, Vanti G, Donato R, Sacco C, Bilia AR. Promising nanocarriers to enhance solubility and bioavailability of Cannabidiol for a Plethora of Therapeutic Opportunities. *Molecules*. 2022;27(18):6070.
23. Franze S, Angelo L, Casiraghi A, Minghetti P, Cilirzo F. Design of liposomal Lidocaine/Cannabidiol fixed Combinations for Local Neuropathic Pain Treatment. *Pharmaceutics*. 2022;14(9):1915.
24. Andriotis EG, Chachlioutaki K, Monou PK, Bouropoulos N, Tzetzis D, Barmalexis P, et al. Development of Water-Soluble Electrospun fibers for the oral delivery of cannabinoids. *AAPS PharmSciTech*. 2021;22(1):23.
25. Bhujbal SV, Mitra B, Jain U, Gong Y, Agrawal A, Karki S, et al. Pharmaceutical amorphous solid dispersion: a review of manufacturing strategies. *Acta Pharm Sinica B*. 2021;11(8):2505–36.
26. Holm TP, Knopp MM, Berthelsen R, Löbmann K. Supersaturated amorphous solid dispersions of celecoxib prepared in situ by microwave irradiation. *Int J Pharm*. 2022;626:122115.
27. Wang X, He S, Wang K, Wang X, Yan T, Yan T, et al. Fabrication of betamethasone micro- and nanoparticles using supercritical antisolvent technology: in vitro drug release study and Caco-2 cell cytotoxicity evaluation. *Eur J Pharm sciences: official J Eur Federation Pharm Sci*. 2023;181:106341.
28. Sabri AH, Kim Y, Marlow M, Scurr DJ, Segal J, Banga AK, et al. Intradermal and transdermal drug delivery using microneedles - fabrication, performance evaluation and application to lymphatic delivery. *Adv Drug Deliv Rev*. 2020;153:195–215.
29. Mangang KN, Thakran P, Halder J, Yadav KS, Ghosh G, Pradhan D et al. PVP-microneedle array for drug delivery: mechanical insight, biodegradation, and recent advances. *J Biomaterials Sci Polym Ed*. 2022;1–32.
30. Lopez-Ramirez MA, Soto F, Wang C, Rueda R, Shukla S, Silva-Lopez C, et al. Built-In active Microneedle Patch with enhanced Autonomous Drug Delivery. *Adv Mater*. 2020;32(1):e1905740.
31. Ke CJ, Lin YJ, Hu YC, Chiang WL, Chen KJ, Yang WC, et al. Multidrug release based on microneedle arrays filled with pH-responsive PLGA hollow microspheres. *Biomaterials*. 2012;33(20):5156–65.
32. Hao G, Xu ZP, Li L. Manipulating extracellular tumour pH: an effective target for cancer therapy. *RSC Adv*. 2018;8(39):22182–92.
33. Boussadia Z, Gambardella AR, Mattei F, Parolini I. Acidic and hypoxic micro-environment in Melanoma: impact of Tumour Exosomes on Disease Progression. *Cells*. 2021;10(12):3311.
34. Dratkiewicz E, Simiczyjew A, Mazurkiewicz Z, Jiętek M, Matkowski R, Nowak D. Hypoxia and extracellular acidification as drivers of Melanoma Progression and Drug Resistance. *Cells*. 2021;10(4):862.
35. Raghunand N, Mahoney BP, Gillies RJ. Tumor acidity, ion trapping and chemotherapeutics II. pH-dependent partition coefficients predict importance of ion trapping on pharmacokinetics of weakly basic chemotherapeutic agents. *Biochem Pharmacol*. 2003;66(7):1219–29.
36. Som A, Raliya R, Tian L, Akers W, Ippolito JE, Singamaneni S, et al. Monodispersed calcium carbonate nanoparticles modulate local pH and inhibit tumor growth in vivo. *Nanoscale*. 2016;8(25):12639–47.
37. Dong Z, Feng L, Hao Y, Chen M, Gao M, Chao Y, et al. Synthesis of Hollow Biomaterialized CaCO<sub>3</sub>-Polydopamine nanoparticles for multimodal imaging-guided Cancer photodynamic therapy with reduced skin photosensitivity. *J Am Chem Soc*. 2018;140(6):2165–78.
38. Chen Q, Wang C, Zhang X, Chen G, Hu Q, Li H, et al. In situ sprayed bioresponsive immunotherapeutic gel for post-surgical cancer treatment. *Nat Nanotechnol*. 2019;14(1):89–97.
39. Boutilier AJ, ElSawa SF. Macrophage polarization States in the Tumor Microenvironment. *Int J Mol Sci*. 2021;22(13):6995.
40. Vitale I, Manic G, Coussens LM, Kroemer G, Galluzzi L. Macrophages and metabolism in the Tumor Microenvironment. *Cell Metabol*. 2019;30(1):36–50.
41. Honarmand M, Namazi F, Mohammadi A, Nazifi S. Can cannabidiol inhibit angiogenesis in colon cancer? *Comp Clin Pathol*. 2019;28(1):165–72.
42. Pathria P, Louis TL, Varner JA. Targeting Tumor-Associated Macrophages in Cancer. *Trends Immunol*. 2019;40(4):310–27.
43. Salter RD, Watkins SC. Dendritic cell altered states: what role for calcium? *Immunol Rev*. 2009;231(1):278–88.
44. Liu H, Shi Y, Qian F. Opportunities and delusions regarding drug delivery targeting pancreatic cancer-associated fibroblasts. *Adv Drug Deliv Rev*. 2021;172:37–51.

## Publisher's Note

Springer Nature remains neutral with regard to jurisdictional claims in published maps and institutional affiliations.